Linear topology in amorphous metal oxide electrochromic networks obtained via low-temperature solution processing

Anna Llordés[1,2]*, Yang Wang[3], Alejandro Fernandez-Martinez[4,5], Penghao Xiao[6], Tom Lee[1,7], Agnieszka Poulain[8], Omid Zandi[3], Camila A. Saez Cabezas[3], Graeme Henkelman[6] and Delia J. Milliron[1,3]*

Amorphous transition metal oxides are recognized as leading candidates for electrochromic window coatings that can dynamically modulate solar irradiation and improve building energy efficiency. However, their thin films are normally prepared by energy-intensive sputtering techniques or high-temperature solution methods, which increase manufacturing cost and complexity. Here, we report on a room-temperature solution process to fabricate electrochromic films of niobium oxide glass (NbO_x) and 'nanocrystal-in-glass' composites (that is, tin-doped indium oxide (ITO) nanocrystals embedded in NbO_x glass) via acid-catalysed condensation of polyniobate clusters. A combination of X-ray scattering and spectroscopic characterization with complementary simulations reveals that this strategy leads to a unique one-dimensional chain-like NbO_x structure, which significantly enhances the electrochromic performance, compared to a typical three-dimensional NbO_x network obtained from conventional high-temperature thermal processing. In addition, we show how self-assembled ITO-in-NbO_x composite films can be successfully integrated into high-performance flexible electrochromic devices.

Amorphous metal oxides films have emerged as an alternative to their crystalline counterparts, because of their compatibility with low-temperature solution processing and strain tolerance, allowing the use of flexible polymeric substrates and high-throughput roll-to-roll fabrication[1–3]. In addition, the intricate structure–property relationships in these amorphous materials, when appropriately controlled, can serve as a handle to tune and enhance functionalities. In particular, electrochemical properties of amorphous transition metal oxides (a-TMO) have been reported to outperform their crystalline counterparts in batteries, supercapacitors and electrochromic devices[4–7]. The improvements were correlated to the local structures of the a-TMOs; for instance, the amorphous structures provided sufficient free volume for ion storage, reducing the activation energy and electrode volume change during ion insertion and extraction[5,8,9]. Similarly, their interstitial space and atomic disorder could act as fast pathways for ion diffusion[10,11]. To manipulate local structure, the inclusion of glass-modifying ions or the presence of embedded crystal–glass interfaces have been shown to result in added free volume following thermal processing[12–14]. But overall, a similar three-dimensional (3D) network topology remains in the amorphous structure.

Here, we show that a dramatically different structure, predominantly chain-like, can result from room-temperature acid-catalysed condensation of metal-oxo clusters. The different network topology strongly influences electrochromic properties of the resultant a-TMO. Amorphous electrochromic films are preferred over crystalline films owing to lower growth temperature, higher coloration efficiency, and greater electrochemical durability[15,16]. In addition, unlike crystalline TMO films, which typically block both near infrared (NIR) and visible light when electrochemically activated, a-TMO films selectively block visible light, enabling dual-band (NIR and visible) light control when combined with NIR-active plasmonic nanocrystals[14,17]. Amorphous TMO electrochromic films are typically deposited by sputtering, which is compatible with plastic substrates such as polyethylene terephthalate (PET), leading to the demonstration of flexible electrochromic devices[18]. However, the high cost and high energy demands of large-scale sputtering equipment and the low sputtering deposition rates for metal oxides have made electrochromic windows expensive to manufacture, which has so far inhibited broad market deployment. Solution deposition could greatly decrease manufacturing cost, since it is performed at ambient pressure and air atmosphere. However, solution deposition methods of a-TMO electrochromic films require high-temperature (typically >300 °C) annealing to achieve reasonable performance. This high temperature precludes the use of PET or similar polymeric substrates[19,20]. Up to now, all reported solution-deposited electrochromic films on flexible substrates have been composed largely or entirely of crystalline particles that are synthesized prior to film deposition; thus, they do not require high-temperature annealing to activate their electrochemical performance[21–23]. This strategy, however, prevents the realization of advantageous a-TMO properties in the resulting devices. Our new processing method
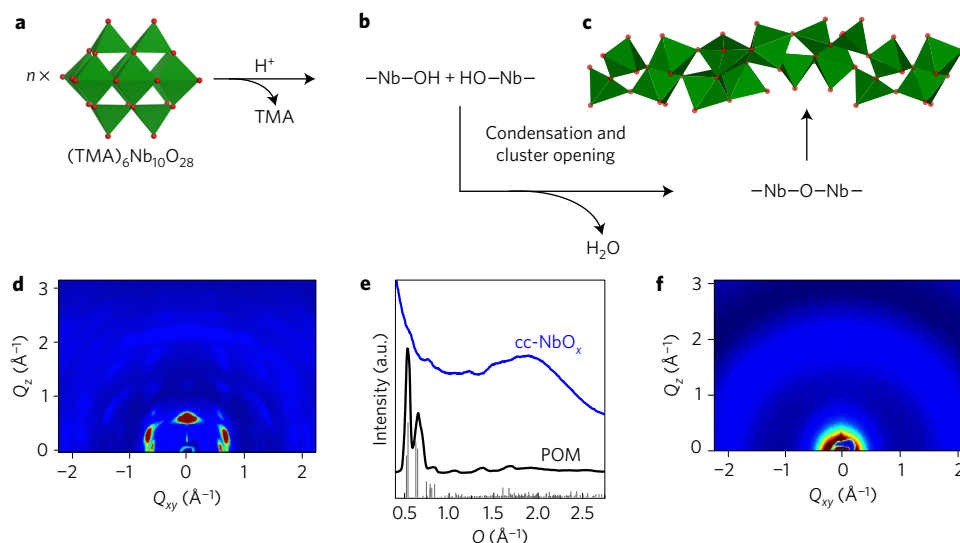
Figure 1 | Chemical condensation of polyniobate cluster (POM) films. a–c, A schematic representation for the chemical condensation process that transforms the POMs (**a**) into an extended NbO_x network (**c**). $[NbO_6]$ octahedra and oxygen atoms are shown in green and red, respectively. **d–f**, Grazing-incidence wide-angle X-ray scattering (GIWAXS) patterns of an as-deposited POM film (**d**) and an amorphous NbO_x film obtained after chemical condensation (**f**). The XRD patterns (**e**) for the POM film (black) and the chemically condensed NbO_x film (blue) were obtained by integrating the 2D images along the out-of-plane scattering direction. The indexed diffraction pattern corresponds to the crystalline POM ICSD#419266. GIWAXS data for thermally condensed NbO_x are shown in Supplementary Fig. 2.

offers the first route to solution process a-TMO electrochromic films compatible with low-temperature substrates.

Specifically, this work reports a route to synthesize amorphous niobium oxide (NbO_x) electrochromic glass thin films via facile solution processing at room temperature. NbO_x films are prepared at ambient conditions by acid-catalysed condensation of niobium polyoxometalates (POMs)[24–26]. Figure 1a–c illustrates the process of chemical condensation. POMs, with composition $[Nb_{10}O_{28}]^{6-}$ and tetramethylammonium (TMA) counterions, were used as precursors to produce amorphous NbO_x films as well as nanocomposite films with embedded tin-doped indium oxide (ITO) nanocrystals (that is, ITO-in-NbO_x composites)[14]. To condense the POM clusters, their spincast films were soaked in a formic acid solution in ethanol (10 vol.%). The protons replace the TMA counterions, protonating the terminal Nb=O bonds and yielding Nb–OH groups, which then undergo a condensation reaction to form bridging Nb–O–Nb bonds between POMs. As a result, an extended disordered NbO_x network is developed. In Fig. 1d–f, grazing-incidence wide-angle X-ray scattering (GIWAXS) patterns (see Methods) show that the POM clusters self-assemble into an ordered molecular film during spincasting[27–29], while chemical condensation transforms this ordered assembly into a randomly oriented amorphous network of NbO_x. We previously reported the preparation of amorphous NbO_x by thermally condensing POM clusters at high temperature ($\sim$400 °C)[14]. In sharp contrast, chemical condensation is performed in solution, and at room temperature, producing uniform and crack-free films (Supplementary Fig. 1), which are beneficial for electrochromic applications, ensuring colour uniformity.

The composition of the chemically condensed NbO_x films (cc-NbO_x) was investigated by Fourier transform infrared (FTIR) spectroscopy and thermogravimetric analysis coupled to mass spectrometry (TGA-MS, Fig. 2a and Supplementary Fig. 3). The FTIR spectrum shows a broad band at 3,300 cm^{-1}, typical of O–H stretching, indicating both the presence of molecular H_2O and Nb–OH groups[30]. The broad distribution of stretching vibrations is ascribed to the exchangeable nature of the OH groups in H_2O, to hydrogen bonding, and to the multiple coordination environments of the hydroxylated groups in the NbO_x matrix[31,32]. The amount of water,

quantified by TGA-MS, was 13% by weight, approximately 2.3 moles per niobium oxide unit formula ($Nb_2O_5 \cdot 2.3H_2O$). TGA-MS also showed 3 wt% of organics, which were identified as residual formate groups left from the acid soaking, in agreement with FTIR (Fig. 2a) ($\sim$0.2 moles per unit formula) (Supplementary Fig. 3). TMA counterions were not detected either by TGA-MS or FTIR, indicating that they were completely removed during the room-temperature condensation process. In sharp contrast, temperatures of at least 400 °C were required to fully decompose TMA counterions when thermally condensing NbO_x films[14].

When subjected to electrochemical cycling in a non-aqueous lithium electrolyte, the hydrous cc-NbO_x is only moderately stable, exhibiting 80% charge capacity fade after 300 cycles (Supplementary Fig. 4). Hypothesizing that absorbed water has a detrimental effect on the electrochemical durability, due to a corrosion effect[33], two methods were investigated to dehydrate the as-prepared cc-NbO_x films at low temperature: annealing in air at 200 °C, and chemical dehydration by a water scavenger—triethyl orthoformate (TEOF)—at 100 °C (see Methods). FTIR showed that both dehydration processes were efficient to remove O–H by $\sim$70% (Fig. 2a). The remaining $\sim$30% O–H stretching peak area can be ascribed to a distribution of Nb–OH groups terminating the internal surface of the NbO_x network, rather than molecular H_2O, based on the presence of Nb–OH bending and absence of H_2O bending signatures in the FTIR (Supplementary Discussion 1). As a result, the dehydrated cc-NbO_x film exhibited much improved electrochemical stability, which is even better than that of thermally condensed (tc) NbO_x (Supplementary Fig. 4).

The local structure of the cc-NbO_x films was investigated by Raman spectroscopy, a technique that can differentiate terminal Nb=O bonds from bridging Nb–O–Nb. Terminal Nb=O bonds have double bond character and appear in the high-frequency region of 800–1,000 cm^{-1} (yellow area in Fig. 2b,c), while bridging Nb–O–Nb bonds appear in a lower-frequency range, 500–800 cm^{-1}. The ratio of the integrated Raman peaks in these two regions reflects the relative abundance of terminal and bridging bonds (T/B) (Fig. 2b and Supplementary Fig. 5 and Supplementary Table 1). For tc-NbO_x, the obtained T/B ratio was $\sim$0.2, indicating a high degree of condensation within the extended bonding structure. The
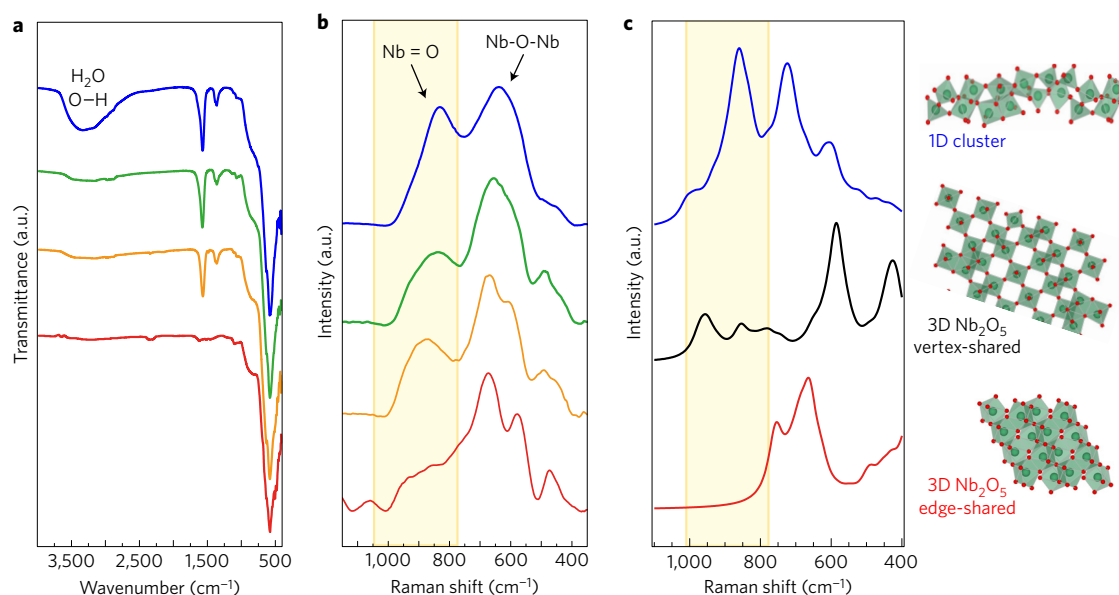
Figure 2 | Compositional and structural analysis of chemically condensed (cc) NbO$_x$ films. a,b, FTIR spectra (**a**) and Raman spectra (**b**) of as-chemically condensed NbO$_x$ (blue), cc-NbO$_x$ after chemical dehydration (green), and cc-NbO$_x$ after thermal dehydration (orange). Thermally condensed (tc) NbO$_x$ film (red) is shown for comparison. In **a**, sharp bands at 1,569 cm^{-1} and 1,377 cm^{-1} correspond to C–O stretching and COO rocking modes of formate. The range 500–800 cm^{-1} is assigned to stretching of Nb–O–Nb bridging bonds, while terminal bonds appear in the range 800–1,000 cm^{-1} (yellow area)[20]. In **b**, the small peak at 1,100 cm^{-1} in the tc film is from fluorescence noise. **c**, Simulated Raman spectra and structural models. From top to bottom: optimized 1D cluster (Nb$_{12}$O$_{44}$H$_{29}$) with a chain-like structure, a monoclinic 3D crystalline H-Nb$_2$O$_5$ (ICSD-29) network with mostly vertex-shared [NbO$_6$] units, and a monoclinic 3D crystalline Z-Nb$_2$O$_5$ (ICSD- 16802) with edge-shared [NbO$_6$] units.

cc-NbO$_x$, in contrast, exhibits a three times larger T/B ratio of ∼0.6, suggesting an exceptionally low degree of condensation and large internal surface area in the amorphous NbO$_x$ network. The T/B ratio decreases after chemical or thermal dehydration, but remains about a factor of two above that for tc-NbO$_x$ (Supplementary Table 1e), indicating that this poorly condensed polymer-like structure persists in the final dehydrated cc-NbO$_x$ films. Similar results were obtained when comparing the Raman spectra of thermally and chemically condensed ITO-in-NbO$_x$ composites (Supplementary Fig. 6).

To gain insight into the structure of the cc-NbO$_x$ beyond the level of individual bonds, X-ray total scattering measurements were performed to generate a pair distribution function (PDF or $G(r)$) for both chemically and thermally condensed NbO$_x$ films as well as for ITO-in-NbO$_x$ films (See Methods)[34]. The probability of finding an atom pair at a given distance for cc-NbO$_x$ and tc-NbO$_x$ is shown in Fig. 3a and Supplementary Fig. 7. The PDF for tc-NbO$_x$ (red curve) shows a peak at 2 Å that corresponds to the Nb–O bond length (r_1), and another peak at 3.3 Å that can be assigned to the Nb–Nb distance between edge-sharing octahedral units. In addition, the Nb–Nb distance between vertex-sharing units appears at 3.8 Å, which is about $2r_1$. Other atom pair correlations appear also at longer distances (4–7 Å), suggesting that tc-NbO$_x$ has a 3D bonding network with a local structure similar to that of crystalline Nb$_2$O$_5$. These similarities can be further appreciated by comparison to the simulated PDF of crystalline Nb$_2$O$_5$ phases (Supplementary Fig. 8)[35].

A different local structure, however, is observed for cc-NbO$_x$ (Fig. 3a, blue curve), in which the peaks at 3.3 Å (indicative of edge-sharing octahedra) and longer distances correlations (4–7 Å) are absent. The reduced structure factor $F(Q)$ for cc-NbO$_x$ shows a distinct two-frequency oscillatory pattern, suggesting the presence of two main atomic correlations (Fig. 3b). These correlations are clearly distinguished in the two PDF peaks (namely, the Fourier-transformed reduced structure factor, Fig. 3a), which correspond to Nb–O and Nb–Nb inter-atomic distances of vertex-sharing

[NbO$_6$] octahedra units (r_1 and ∼$2r_1$). Therefore, a qualitative analysis of the total scattering data indicates that the amorphous cc-NbO$_x$, obtained from the room-temperature condensation of POM clusters, has a linear type of structure (see Supplementary Discussion 2 and Supplementary Fig. 9), which is in agreement with the low degree of network condensation (that is, high content of terminal Nb=O bonds) observed by Raman spectroscopy. This unique 1D topology forms even when ITO nanocrystals are embedded in the glassy NbO$_x$ matrix (Fig. 3c). These nanocrystal-in-glass composites were obtained analogously by chemically condensing ITO–POM films at room temperature (see Methods). The reduced structure factor $F(Q)$ of a ITO-in-NbO$_x$ composite and that of a reference sample containing only ITO nanocrystals are shown in Fig. 3c. The difference between the two $F(Q)$ traces yields the reduced structure factor of the NbO$_x$ amorphous matrix (in light blue), which agrees well with the $F(Q)$ of the pure cc-NbO$_x$ (dark blue), thus indicating a similar 1D chain-like structure.

To further interpret the structural differences of the two amorphous polymorphs, tc-NbO$_x$ and cc-NbO$_x$, computational structure optimization based on density functional theory (DFT) was used to generate a physically meaningful structure for cc-NbO$_x$ that accounts for the observed Raman and PDF features. Using the empirically determined 1D structure (Supplementary Fig. 9) as a starting point, DFT, as implemented in the Vienna Ab-initio Simulation Package (VASP) with the Perdew–Burke–Ernzerhof (PBE) functional[36,37], was used to define the forces between the atoms (see Methods). Candidate structures were subjected to molecular dynamics (MD) sampling, followed by local energy minimization to relax the structure. This approach goes beyond fitting methods that may be sufficient for small local perturbations from known crystalline structures[38], but that can yield unphysical results for truly amorphous materials (see Supplementary Discussion 2).

The computationally determined structure consists of a 1D chain structure with the composition of Nb$_{12}$O$_{44}$H$_{29}$ (Fig. 3d). From this structure, a PDF (Fig. 3d) and a Raman spectrum
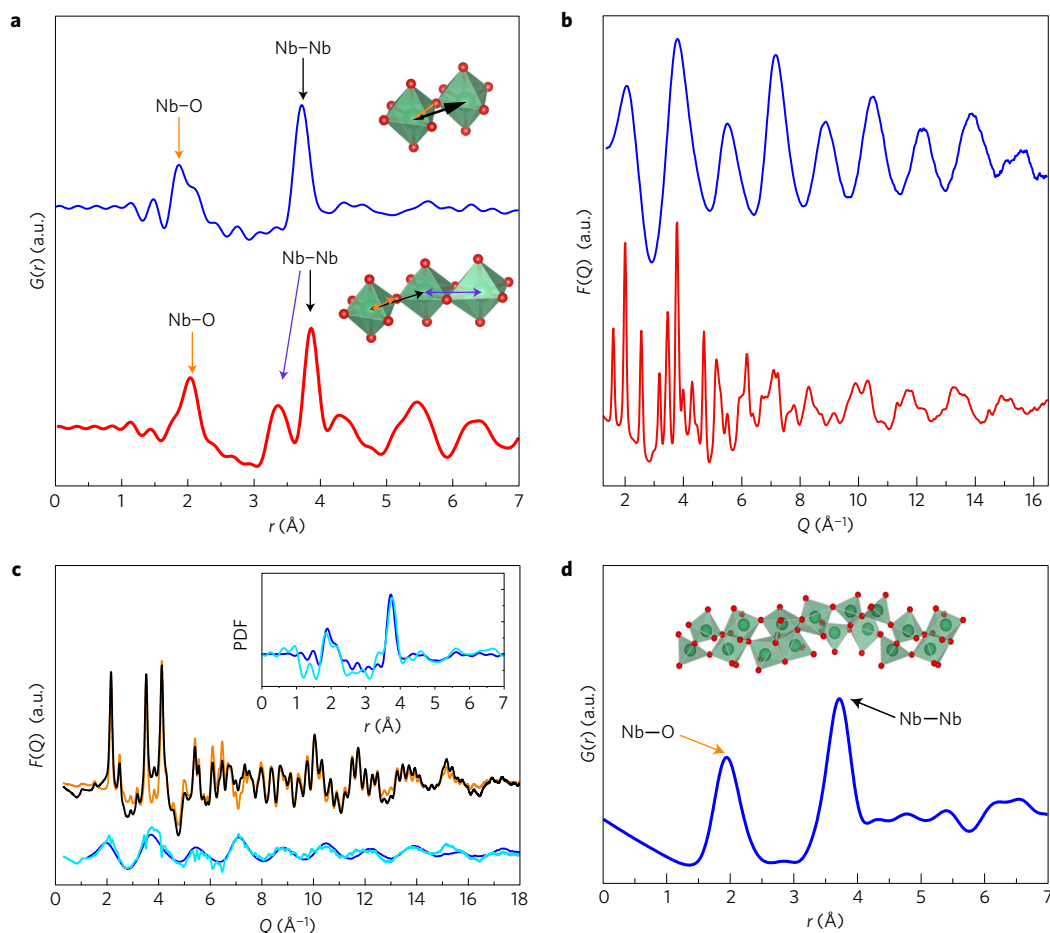
Figure 3 | Characterization of local structure. a, Pair distribution function (PDF, or $G(r)$) of amorphous NbO_x networks obtained by chemical condensation (cc) in blue, and thermal condensation (tc) in red. The inset shows the possible octahedral arrangements for cc-NbO_x (top) and tc-NbO_x (bottom). The orange, purple and black arrows indicate the atomic distances for Nb–O, edge-sharing Nb–Nb and vertex-sharing Nb–Nb, respectively. **b**, Reduced structure factor $F(Q)$ of cc-NbO_x (in blue) and tc-NbO_x (in red). **c**, $F(Q)$ of a ITO-in-NbO_x cc-nanocomposite sample (in black). A reference sample containing only ITO nanocrystals is shown in orange. The difference between the two $F(Q)$ data yields the $F(Q)$ of the NbO_x amorphous matrix (in light blue), which agrees well with the $F(Q)$ of the cc-NbO_x measured independently (dark blue). Inset shows a zoomed-in view of their PDF. **d**, Simulated PDF and computationally determined structural model for cc-NbO_x. The same model was used for simulating the Raman spectrum (Fig. 2c, blue trace). Experimental PDF for the POM clusters, before condensation, is shown in Supplementary Fig. 10.

(Fig. 2c) were generated. For comparison, two monoclinic and one tetragonal Nb_2O_5 crystalline phases (Supplementary Fig. 8), which contain a variable ratio of vertex-sharing and edge-sharing octahedra, were considered to mimic the range of local structures possible in tc-NbO_x. Compared to those crystalline Nb_2O_5 models with 3D topology (Supplementary Fig. 8), the simulated PDF for cc-NbO_x (Fig. 3d) lacks the edge-sharing Nb–Nb peak at 3.3 Å and long-distance atomic correlations and ordering (4–7 Å), which is consistent with the experimental results (Fig. 3a). It is noteworthy that the edge-sharing Nb–Nb peak not found in cc-NbO_x still exists in H-Nb_2O_5 and Z-Nb_2O_5 even when all the oxygen atoms are removed, thus confirming this signal is not from other atom pairs, such as Nb–O distance across neighbouring units. In addition, the simulated Raman spectrum (Fig. 2c) for the 1D model shows a strong peak in the high-frequency region (800 cm^{-1}–1,000 cm^{-1}), which is absent for the bulk crystalline structures. This observation is in excellent agreement with the experimental data (Fig. 2b), as this signal is attributed to the abundant terminal Nb=O bonds in cc-NbO_x. Therefore, the combined experimental and theoretical analysis indicates that chemical condensation affords a disordered chain-like NbO_x structure with primarily vertex-sharing [NbO_6] units, confirming the qualitative interpretations of the PDF and Raman data. In addition, the DFT-based simulations validate that

the proposed structure is a physically realistic representation of cc-NbO_x local structure.

The mechanism of formation of such 1D topology in the amorphous NbO_x structure can be rationalized by cluster-opening reactions, structural rearrangements and lateral condensation of [NbO_6] units in POMs[39,40]. The resulting lower dimensionality of the local structure can potentially have a strong influence on the electrochemical properties of NbO_x. It has been reported that 2D layered metal oxides, such as exfoliated WO_3 nanosheets, can exhibit faster electrochemical kinetics and higher charge capacity than their 3D counterparts[41–43].

To explore this hypothesis, the change in optical transmission upon electrochemical charging was investigated for cc-NbO_x and tc-NbO_x films (Fig. 4a). The tc-NbO_x film has a low-energy absorbance peak centred at 900 nm, which grows with inserted charge, while this peak is absent for cc-NbO_x. This difference can be attributed to the less condensed network of cc-NbO_x, so the polaronic states are restricted to more localized spatial extent than in tc-NbO_x, where larger polarons may coexist with highly localized charges[20,44,45]. This comparison also shows that the cc-NbO_x film generates a higher optical modulation (ΔA) in the visible range than the tc-NbO_x when the same charge density (ΔQ) is inserted, indicating higher coloration efficiency
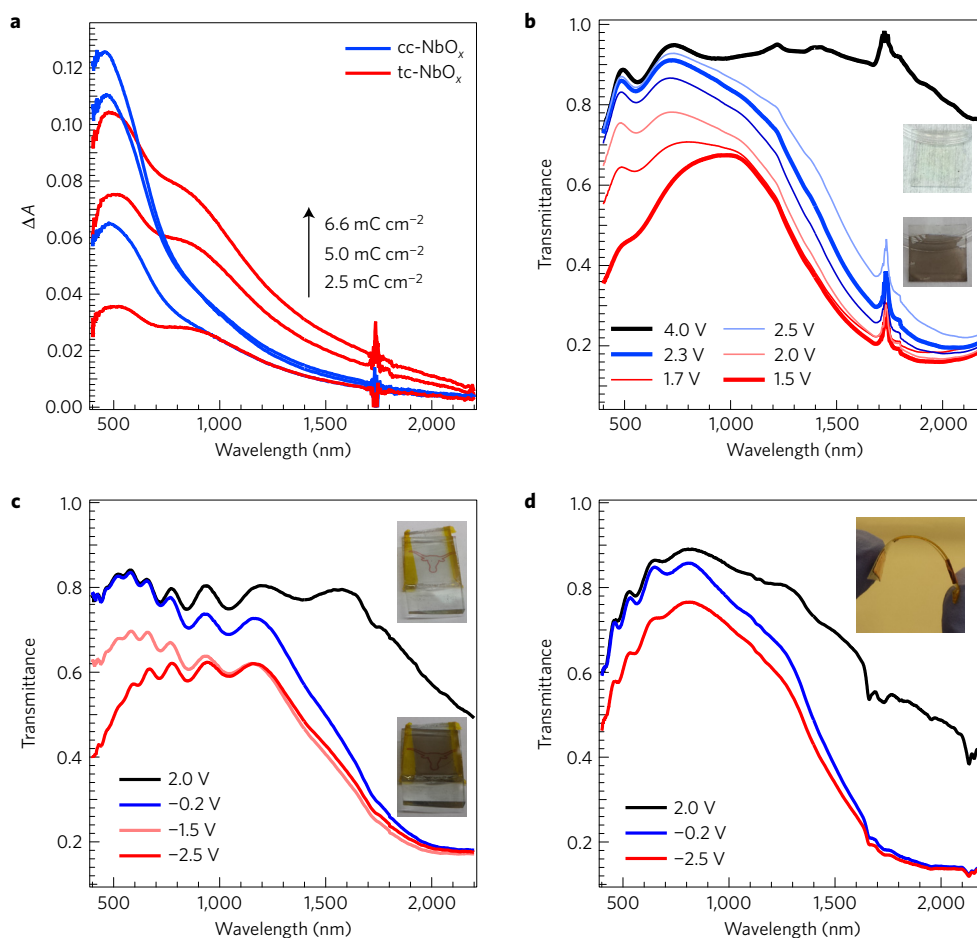
Figure 4 | Spectroelectrochemical measurements for chemical-condensed films and devices. a, Differential absorbance spectra of cc-NbO$_x$ and tc-NbO$_x$ films at 1.5 V versus Li/Li$^+$, at various levels of inserted charge. From bottom to top, the three spectra in each colour were recorded at a charge density of 2.5, 5.0 and 6.6 mC cm^{-2}. The film thickness was 100 ± 10 nm for both samples. All the spectra were baselined against their own spectra at 4.0 V (the transparent state). **b**, Electrochromic performance for a chemically condensed ITO-in-NbO$_x$ composite film under different applied voltages (half-cell measurements in liquid electrolyte. See Methods). Each voltage was held constant for 2 min, except 5 min and 10 min for 1.7 V and 1.5 V, respectively. The photographs show the visual colour change for the composite film on ITO-coated glass when switched from a transparent mode (at 4.0 V) to a dark mode (at 1.5 V). The film thickness is ∼300 nm. **c,d**, Electrochromic performance for a full solid-state electrochromic device fabricated on fluorine-doped tin oxide (FTO)-coated glass (**c**) and PET flexible substrates (**d**). Each voltage was held constant for 5 min, except 10 min for −2.5 V. The photographs in **c** show the colour change of the device when switched from the transparent state to the dark state. The inset photograph in **d** shows a flexible device when bent.

(CE) for the cc-NbO$_x$. Defined as CE = $\Delta A/\Delta Q$, this figure of merit can be determined by fitting the linear region in the plot of ΔA versus ΔQ, and extracting the slope. The cc-NbO$_x$ film has a CE of ∼30 cm^2/C, which is twice that of the tc-NbO$_x$ film (∼15 cm^2/C) (Supplementary Fig. 11). Analogous to crystalline Nb$_2$O$_5$ phases with 2D layered structures[46], the inter-chain space in the cc-NbO$_x$ may provide fast channels for ion intercalation and diffusion. Additionally, in 2D TMO nanosheets, terminal M=O groups have been shown to be electrochemical active sites that effectively lower the activation energy for Li$^+$ intercalation[41], a role that may be played by the abundant terminal Nb=O bonds in our cc-NbO$_x$. In other words, the colour centre in NbO$_x$ is more accessible in a 1D topology than in a 'fully condensed' 3D network. The kinetics of ion insertion were evaluated by electrochemical impedance spectroscopy (Supplementary Fig. 12). The resultant Li$^+$ diffusion coefficient for cc-NbO$_x$ is two orders of magnitude higher than that for tc-NbO$_x$.

The acid-catalysed condensation process enables integration of cc-NbO$_x$ into composite materials and electrochromic devices, even on flexible polymeric substrates. Composite nanocrystal-in-glass electrochromic films, capable of modulating both visible and NIR light, can be made by embedding ITO nanocrystals in NbO$_x$

glass, as we previously reported by using a thermal condensation process[14]. The analogous chemically condensed composite prepared here exhibits strong and selective dual-band modulation in the visible and NIR spectral ranges (Fig. 4b) that is comparable to that for a thermally condensed composite annealed at 400 °C (ref. 14). The plasmonic electrochromic response of the ITO nanocrystals controls NIR light transmission without affecting the visible transmittance[16]. The NbO$_x$ becomes reduced at lower potentials than ITO, generating polaronic absorption, modulating the transmittance of the visible light and thus darkening the film (Fig. 4b). The electrochemical cyclability for the cc-composite is excellent, with only about 5% of optical and charge capacity fade after 1,000 cycles, which is superior to the stability of individual NbO$_x$ and ITO nanocrystal films (Supplementary Fig. 13). In addition, the relative modulation of visible and NIR light can be tuned by varying the ITO nanocrystal volume ratio in the composite film (Supplementary Figs 14 and 15).

A solid-state electrochromic device based on chemically condensed ITO-in-NbO$_x$ composite was fabricated with a Li-ion conducting polymeric electrolyte and a CeO$_2$ nanocrystal counter electrode for charge storage (see Methods)[47,48]. CeO$_2$ is optically passive, thus avoiding interference with the dual-band

electrochromic response of the ITO-in-NbO$_x$ composite. Similar to the half-cell results (Fig. 4b), the full device also exhibits strong dual-band modulation with selective control of the transmittance in the visible and NIR region (Fig. 4c). This device can be cycled at least 1000 times between 2 V (bright) and −2.5 V (dark) (Supplementary Fig. 16). A key advantage of the low-temperature process is the compatibility with flexible polymeric substrates, so a similar device was fabricated using ITO-coated PET substrates. The flexible device exhibits dual-band electrochromic behaviour under similar biases (Fig. 4d). However, the visible modulation is weaker than that of the rigid device. This difference is mainly due to the limited film thickness of the CeO$_2$ counter electrode fabricated on PET, as thermal stability of the PET substrate is not sufficient to afford repeated coating and thermal annealing at 150 °C, which is necessary for obtaining an optimally thick CeO$_2$ film. Despite the counter electrode limitation, this flexible device demonstrates the practical advantage of chemical condensation to enable new form factors of dual-band electrochemical devices.

In summary, this work examines two distinct electrochromic amorphous polyamorphs of NbO$_x$. In particular, the one synthesized by room-temperature, acid-catalysed condensation of POMs results in a 1D network topology with an abundant internal surface of terminal Nb=O bonds. These unique structural features at the local scale directly correlate to the enhanced electrochemical properties. This low-temperature processing strategy has been extended to dual-band nanocrystal-in-glass electrochromics and can be applicable to other a-TMOs. It also opens new avenues for integrating materials into synergistic composites and novel form factor devices that can have applications beyond electrochromics. Broadly, this work highlights the great potential for materials discovery by studying the local structure–property relations of a-TMOs.

Methods

Methods and any associated references are available in the [online version of the paper](#).

References

1. Kim, Y.-H. *et al*. Flexible metal-oxide devices made by room-temperature photochemical activation of sol–gel films. *Nature* **489,** 128–132 (2014).
2. Banger, K. K. *et al*. Low-temperature, high-performance solution-processed metal oxide thin-film transistors formed by a 'sol–gel on chip' process. *Nat. Mater.* **10,** 45–50 (2011).
3. Kim, M-G., Kanatzidis, M. G., Facchetti, A. & Marks, T. J. Low-temperature fabrication of high-performance metal oxide thin-film electronics via combustion processing. *Nat. Mater.* **10,** 382–388 (2011).
4. Granqvist, C. G. Electrochromics for smart windows: Oxide-based thin films and devices. *Thin Solid Films* **564,** 1–38 (2014).
5. Legrain, F., Malyi, O. & Manzhos, S. Insertion energetics of lithium, sodium, and magnesium in crystalline and amorphous titanium dioxide: a comparative first-principles study. *J. Power Sources* **278,** 197–202 (2015).
6. Chae, O. B. *et al*. Reversible lithium storage at highly populated vacant sites in an amorphous vanadium pentoxide electrode. *Chem. Mater.* **26,** 5874–5881 (2014).
7. Colton, R. J., Guzman, A. M. & Rabalais, J. W. Photochromism and electrochromism in amorphous transition metal oxide films. *Acc. Chem. Res.* **11,** 170–176 (1978).
8. Jang, J. *et al*. Electrode performances of amorphous molybdenum oxides of different molybdenum valence for lithium-ion batteries. *Isr. J. Chem.* **55,** 604–610 (2015).
9. Ku, J. H., Ryu, J. H., Kim, S. H., Han, O. H. & Oh, S. M. Reversible lithium storage with high mobility at structural defects in amorphous molybdenum dioxide electrode. *Adv. Funct. Mater.* **22,** 3658–3664 (2012).
10. Uchaker, E. *et al*. Better than crystalline: amorphous vanadium oxide for sodium-ion batteries. *J. Mater. Chem. A* **2,** 18208–18214 (2014).
11. Lee, J. *et al*. Unlocking the potential of cation-disordered oxides for rechargeable lithium batteries. *Science* **343,** 519–522 (2014).
12. Shelby, J. E. *Introduction to Glass Science and Technology* (Royal Society of Chemistry, 2005); http://dx.doi.org/10.1039/9781847551160
13. Sakamoto, A. & Yamamoto, S. Glass-ceramics: engineering principles and applications. *Int. J. Appl. Glass Sci.* **1,** 237–247 (2010).
14. Llordes, A., Garcia, G., Gazquez, J. & Milliron, D. J. Tunable near-infrared and visible-light transmittance in nanocrystal-in-glass composites. *Nature* **500,** 323–326 (2013).
15. Granqvist, C. G. Electrochromic tungsten oxide films: review of progress 1993–998. *Sol. Energy Mater Sol. Cells* **60,** 201–262 (2000).
16. Runnerstrom, E. L., Llordes, A., Lounis, S. D. & Milliron, D. J. Nanostructured electrochromic smart windows: traditional materials and NIR-selective plasmonic nanocrystals. *Chem. Commun.* **50,** 10555–10572 (2014).
17. Kim, J. *et al*. Nanocomposite architecture for rapid, spectrally-selective electrochromic modulation of solar transmittance. *Nano Lett.* **15,** 5574–5579 (2015).
18. Granqvist, C. G. *et al*. Electrochromic foil-based devices: Optical transmittance and modulation range, effect of ultraviolet irradiation, and quality assessment by $1/f$ current noise. *Thin Solid Films* **516,** 5921–5926 (2008).
19. Arakaki, J., Reyes, R., Horn, M. & Estrada, W. Electrochromism in NiO$_x$ and WO$_x$ obtained by spray pyrolysis. *Sol. Energy Mater Sol. Cells* **37,** 33–41 (1995).
20. Orel, B., Maček, M., Grdadolnik, J. & Meden, A. *In situ* UV-Vis and *ex situ* IR spectroelectrochemical investigations of amorphous and crystalline electrochromic Nb$_2$O$_5$ films in charged/discharged states. *J. Solid State Electrochem.* **2,** 221–236 (1998).
21. Costa, C., Pinheiro, C., Henriques, I. & Laia, C. A. T. Inkjet printing of sol-gel synthesized hydrated tungsten oxide nanoparticles for flexible electrochromic devices. *ACS Appl. Mater. Interfaces* **4,** 1330–1340 (2012).
22. Mihelčič, M. *et al*. Comparison of electrochromic properties of Ni$_{1-x}$O in lithium and lithium-free aprotic electrolytes: From Ni$_{1-x}$O pigment coatings to flexible electrochromic devices. *Sol. Energy Mater Sol. Cells* **120,** 116–130 (2014).
23. Layani, M. *et al*. Nanostructured electrochromic films by inkjet printing on large area and flexible transparent silver electrodes. *Nanoscale* **6,** 4572–4576 (2014).
24. Ohlin, C. A., Villa, E. M. & Casey, W. H. One-pot synthesis of the decaniobate salt [N(CH$_3$)$_4$]$_6$[Nb$_{10}$O$_{28}$]· 6H$_2$O from hydrous niobium oxide. *Inorg. Chim. Acta* **362,** 1391–1392 (2009).
25. Villa, E. M. *et al*. Reaction dynamics of the decaniobate ion [H$_x$Nb$_{10}$O$_{28}$]$^{(6−x)−}$ in water. *Angew. Chem. Int. Ed. Engl.* **47,** 4844–4846 (2008).
26. Hou, Y., Zakharov, L. N. & Nyman, M. Observing assembly of complex inorganic materials from polyoxometalate building blocks. *J. Am. Chem. Soc.* **135,** 16651–16657 (2013).
27. Wang, Y. & Weinstock, I. A. Cation mediated self-assembly of inorganic cluster anion building blocks. *Dalton Trans.* **39,** 6143–6152 (2010).
28. Wang, Y. *et al*. Self-assembly and structure of directly imaged inorganic-anion monolayers on a gold nanoparticle. *J. Am. Chem. Soc.* **131,** 17412–17422 (2009).
29. Musumeci, C., Luzio, A. & Pradeep, C. P. Programmable surface architectures derived from hybrid polyoxometalate-based clusters. *J. Phys. Chem. C* **115,** 4446–4455 (2011).
30. Livage, J. Vanadium pentoxide gels. *Chem. Mater.* **3,** 578–593 (1991).
31. Boily, J.-F. & Felmy, A. R. On the protonation of oxo- and hydroxo-groups of the goethite (α-FeOOH) surface: A FTIR spectroscopic investigation of surface O–H stretching vibrations. *Geochim. Cosmochim. Acta* **72,** 3338–3357 (2008).
32. Tsyganenko, A. A. & Filimonov, V. N. Infrared spectra of surface hydroxyl groups and crystalline structure of oxides. *J. Mol. Struct.* **19,** 579–589 (1973).
33. Judeinstein, P., Morineau, R. & Livage, J. Electrochemical degradation of WO$_3$· nH$_2$O thin films. *Solid State Ion.* **51,** 239–247 (1992).
34. Cliffe, M. J., Dove, M. T., Drabold, D. A. & Goodwin, A. L. Structure determination of disordered materials from diffraction data. *Phys. Rev. Lett.* **104,** 125501 (2010).
35. McConnell, A. A., Aderson, J. S. & Rao, C. N. R. Raman spectra of niobium oxides. *Spectrochim. Acta Mol. Biomol. Spectrosc.* **32,** 1067–1076 (1976).
36. Fonari, A. & Stauffer, S. *Raman Off-Resonant Activity Calculator Using VASP as a Back-end* vasp_raman.py (2013); https://github.com/raman-sc/VASP
37. Granlund, L., Billinge, S. J. L. & Duxbury, P. M. Algorithm for systematic peak extraction from atomic pair distribution functions. *Acta Crystallogr. Sect. A* **71,** 392–409 (2015).
38. McGreevy, R. L. Reverse Monte Carlo modelling. *J. Phys.: Condens. Matter.* **13,** R877–R913 (2001).
39. Rustad, J. R. & Casey, W. H. Metastable structures and isotope exchange reactions in polyoxometalate ions provide a molecular view of oxide dissolution. *Nat. Mater.* **11,** 223–226 (2012).
40. Chemseddine, A. & Bloeck, U. How isopolyanions self-assemble and condense into a 2D tungsten oxide crystal: HRTEM imaging of atomic arrangement in an intermediate new hexagonal phase. *J. Solid State Chem.* **181,** 2731–2736 (2008).
41. Liang, L. *et al*. High-performance flexible electrochromic device based on facile semiconductor-to-metal transition realized by WO$_3$· 2H$_2$O ultrathin nanosheets. *Sci. Rep.* **3,** 1936 (2013).

42. Miyauchi, M., Kondo, A., Atarashi, D. & Sakai, E. Tungstate nanosheet ink as a photonless and electroless chromic device. *J. Mater. Chem. C* **2,** 3732–3737 (2014).

43. Wu, C. *et al*. Two-dimensional vanadyl phosphate ultrathin nanosheets for high energy density and flexible pseudocapacitors. *Nat. Commun.* **4,** 2431 (2013).

44. Triana, C. A., Granqvist, C. G. & Niklasson, G. A. Electrochromism and small-polaron hopping in oxygen deficient and lithium intercalated amorphous tungsten oxide films. *J. Appl. Phys.* **118,** 024901 (2015).

45. Triana, C. A., Granqvist, C. G. & Niklasson, G. A. Optical absorption and small-polaron hopping in oxygen deficient and lithium-ion-intercalated amorphous titanium oxide films. *J. Appl. Phys.* **119,** 015701 (2016).

46. Lubimtsev, A. A., Kent, P. R. C., Sumpter, B. G. & Ganesh, P. Understanding the origin of high-rate intercalation pseudocapacitance in Nb_2O_5 crystals. *J. Mater. Chem. A* **1,** 14951–14956 (2013).

47. Wang, Y., Runnerstom, E. L. & Milliron, D. J. Switchable materials for smart windows. *Annu. Rev. Chem. Biomol. Eng.* **7,** 283–304 (2016).

48. Williams, T. E. *et al*. NIR-Selective electrochromic heteromaterial frameworks: a platform to understand mesoscale transport phenomena in solid-state electrochemical devices. *J. Mater. Chem. C* **2,** 3328–3335 (2014).

Author contributions

A.L. and Y.W. contributed equally to this work. A.L., Y.W. and T.L. synthesized the materials, carried out the experiments, and analysed the data. P.X. and G.H. performed the DFT simulations. A.F.-M. and A.P. conducted the PDF measurements, data analysis, and interpretation. O.Z. and C.S.C. conducted the EIS and the Raman measurements, respectively. A.L., Y.W. and D.J.M. were responsible for experimental design and wrote the manuscript, which incorporates critical input from all authors.

Additional information

Supplementary information is available in the online version of the paper. Reprints and permissions information is available online at www.nature.com/reprints. Correspondence and requests for materials should be addressed to A.L. or D.J.M.

Competing financial interests

D.J.M. has a financial interest in Heliotrope Technologies, a company pursuing commercial development of electrochromic devices.

Methods

Materials and film preparation. The synthesis of decaniobate POM clusters, namely $(N(CH_3)_4)_6Nb_{10}O_{28} \cdot 14H_2O$, and that of ITO plasmonic nanocrystals and POM–ITO composite solutions were performed as reported previously[14,49]. A typical solution of decaniobate POM was prepared by dissolving 40 mg of $(N(CH_3)_4)_6Nb_{10}O_{28} \cdot 14H_2O$ in 1 ml of solvent mixture ethanol/water (7:3). 20 μl of this POM solution was then deposited on a 2 cm × 2 cm conducting glass substrate (ITO-coated glass with sheet resistance of 20 Ω/sq) or on a flexible plastic substrate (ITO-coated polyethylene terephthalate (PET) with sheet resistance of 60 Ω/sq). Both conducting substrates were commercially available. Before the deposition, the substrates were first thoroughly cleaned with 2 vol.% alkaline aqueous solution (Hellmanex III), rinsed with deionized water (10–15 times), then washed with acetone, and finally with isopropanol. The substrates were further cleaned with ultraviolet-ozone, a photo-sensitized oxidation process that ensured a hydrophilic surface and hence good wetability of the aqueous-based POM solutions. Typically, a 200-nm-thick POM film was obtained from depositing a 40 mg ml^{-1} POM solution at a spin rate of 2,000 r.p.m. for 2 min, followed by a final segment at 6,000 r.p.m. for 45 s. Film thickness was measured by profilometry. A similar procedure was used to deposit POM–ITO composite films from POM–ITO colloidal solutions.

Chemical condensation film processing. The as-deposited POM and POM–ITO films were soaked for 10 min in a formic acid solution (10% by volume) in anhydrous ethanol, at room temperature. Shorter times and lower acid concentrations also resulted in condensation of the POM network, but the aforementioned conditions were used in all experiments. After chemically condensing the films in the acidic solution, they were rinsed with ethanol (three times) and dried at room temperature.

Water-removal film processing. Two methods were used to dehydrate the chemically condensed films: thermal treatment at 200 °C for an hour; and chemical treatment using triethyl orthoformate (TEOF) as a water scavenger. The latter process was carried out by soaking the as-prepared chemically condensed film in pure TEOF for 72 hours at 100 °C. Solutions of TEOF in acetonitrile were also effective to remove water.

Structural and chemical characterization. *TGA-MS.* The composition of the chemically condensed films was investigated by thermogravimetric and evolved gas analysis (Supplementary Fig. 3). The experiments were performed under flowing air gas (25 ml min^{-1}) using a TA instrument model Q5000 coupled with a Pfeiffer Thermostar mass spectrometer.

FTIR. The composition of the chemically condensed films was also investigated by FTIR, using a Perkin Elmer Spectrum One spectrometer. The sample-holder compartment was purged with dried nitrogen for 45 min to ensure complete removal of moisture and, thus accurate identification of water signals from the sample. All spectra were collected in transmission mode by accumulation of 16 scans with 8 cm^{-1} resolution from 400 to 4,000 cm^{-1}. To study the evolution of water-removal processing, the same sample and the same spatial location was used to collect the data and to do further treatment.

Grazing-incidence wide-angle X-Ray scattering (GIWAXS). Thin-film GIWAXS data shown in Fig. 1d–f were acquired at Stanford Synchrotron Radiation Lightsource (SSRL), beamline 11–3 with $\lambda = 0.974$ Å. Acquisitions were performed in grazing-incidence mode (incidence angle = 0.12°) to avoid the signal from the substrate. The scattered X-rays were collected with an area detector.

Scanning electron microscopy. SEM imaging (Supplementary Fig. 1) was carried by means of a Zeiss Gemini Ultra-55 microscope, using beam energies of 5–10 kV and an In-Lens detector.

Raman spectroscopy. The bonding arrangement of the condensed POM films was studied by Raman spectroscopy (Supplementary Fig. 5 and Supplementary Table 1), using a Horiba LabRAM Aramis instrument with confocal aperture. All Raman spectra were obtained with a ×100 microscope objective (numerical aperture = 0.90), 17.7 mW of laser power at excitation wavelength of 532 nm and an acquisition time of 180 s. The spectral resolution was 1.5 cm^{-1} and the laser spot size ∼721 nm. Several spots were examined on each sample and showed similar spectra. Raman peaks from the substrate appeared in a different spectral region than for NbO$_x$, allowing accurate data interpretation. Note that the cross-section for Raman scattering can intrinsically differ between terminal and bridging bonds, and thus peak fitting and integration does not offer a quantitative determination for the ratio of terminal and bridging bonds in a certain sample. However, the peak ratios can be compared between differently prepared amorphous films to inform understanding of structural differences. In this context, the theoretical results that simulate the Raman spectra for different structural motifs provide a critical validation of the qualitative interpretation made by peak fitting.

X-ray total scattering and pair distribution function (PDF) analysis. X-ray total scattering experiments were performed at beamline ID15B of the European Synchrotron Radiation Facility (ESRF, Grenoble, France). Given that total scattering experiments require a certain mass of material (∼50 mg), powders were used instead of thin films. The composition and structure of condensed films versus condensed powders were found to be indistinguishable by TGA-MS, FTIR and Raman spectroscopy. Therefore, we assume that the local structure of the powders resembles that of the films.

Powder samples were loaded in Kapton capillaries. An incident X-ray wavelength of $\lambda = 0.1411$ Å was selected, allowing for a Q-range from 1 to 23 Å^{-1}. The X-ray wavelength was calibrated with a CeO$_2$ standard. The scattered radiation was collected with a Perkin Elmer flat panel detector. Two-dimensional images were integrated and corrected for non-detector orthogonality using Fit2D[50]. Pair distribution functions, $G(r)$, (or PDFs), were generated from total scattering data using the PDFGetX3 software[51]. The PDF, $G(r)$, is related mathematically to the reduced structure factor, $F(Q)$ as follows:

$$F(Q) = Q[S(Q) - 1] \tag{1}$$

$$G(r) = 4\pi r \rho_0(g(r) - 1) = \frac{2}{\pi} \int_0^\infty Q[S(Q) - 1] \sin(Qr)\, dQ \tag{2}$$

in which $S(Q)$ is the total scattering function.

PDF and Raman simulations. Starting with a test structure that was constructed by qualitatively analysing the experimental PDF peak intensity and positions (see further details in Supplementary Discussion 2), molecular dynamics (MD) based on DFT was used to generate the structure of the cc-NbO$_x$. All DFT calculations were performed with the plane wave basis set as implemented in VASP. The generalized gradient approximation (GGA) with the Perdew–Burke–Ernzerhof formula (non-hybrid) was employed for the exchange correlation energy. Core electrons were described by the projector augmented wave method (PAW) for computational efficiency. PDF was simulated using the DiffPy-CMI package[37,52]. The Raman spectra were simulated by taking the derivative of the polarizability along each phonon mode using VASP invoked by the vasp_raman python script[36].

Electrochromic and electrochemical testing (half-cell measurements). The optical switching properties were tested in an argon glove box, using a in-house-built spectroelectrochemical (SEC) cell. The SEC cell had a three-electrode configuration, with Li foils as counter and reference electrodes, the electrolyte being 0.1 M LiTFSI (lithium bis-trifluoromethanesulfonimide) in anhydrous tetraglyme. The condensed POM film was placed as the working electrode and *in situ* transmission spectra were recorded (ASD Quality Spec Pro visible-NIR spectrometer) as a function of the applied potential (Bio-logic VSP potentiostat). Cyclic voltammetry measurements were performed in a in-house-built thin-film electrochemical cell that ensured a constant area of contact with the electrolyte solution. Electrochemical impedance spectroscopy (EIS) measurements were carried out using a frequency range of 0.1 Hz–100 kHz with an a.c. amplitude of 40 mV with a Li foil as both the counter and reference electrodes. To measure the Li$^+$ diffusion coefficient, electrodes were charged to an identical charge state and allowed to equilibrate to open circuit voltage (OCV), after which EIS was carried out using the corresponding OCV as the DC bias.

Preparation of CeO$_2$ counter electrode materials. CeO$_2$ nanocrystals (NCs) were synthesized at 180 °C and then ligand-stripped at room temperature following previously published procedures[49,53]. The ligand-stripped CeO$_2$ NCs were finally dispersed in dimethylformamide (DMF). Then, an Elcometer 4340 blade coater was used to deposit CeO$_2$ NC thin films onto a clean FTO glass substrate or ITO/PET polymeric substrate at a chuck temperature of 50 °C. The coating process was repeated ∼10 times to reach a film thickness of ∼1 μm, and a thermal annealing step at 150 °C for 30 min was applied after each deposition. Finally, the CeO$_2$ counter electrode was electrochemically charged in a 0.1 M LiTFSI/tetraglyme bath at 1.5 V versus Li/Li$^+$ to store charge for device switching.

Preparation and characterization of electrochromic devices on glass substrates and flexible polymer substrate. The solid-state devices were fabricated in the argon-filled glove box by laminating the working electrode and counter electrode together with an interlayer of polymer gel electrolyte. The electrolyte, containing poly(methyl methacrylate) (PMMA), LiTFSI, and tetraglyme, was selected because of the good Li-ion conductivity at room temperature, electrochemical stability, and optical transparency in both visible and NIR spectral ranges. This polymer gel electrolyte was first doctor-bladed onto the NbO$_x$-ITO working electrode. Then, the charged CeO$_2$ electrode was directly placed on top of the electrolyte-coated working electrode, and the assembled device was laminated under vacuum at 90 °C for 30 min. The final device had an active area of ∼3 cm^2. The device was characterized with the same spectrometer and potentiostat as used for half-cell

measurements. The potential applied on the working electrode was referenced to the CeO_2 counter electrode.

References

49. Llordes, A. *et al*. Polyoxometalates and colloidal nanocrystals as building blocks for metal oxide nanocomposite films. *J. Mater. Chem.* **21,** 11631–11638 (2011).
50. Hammersley, A. P., Svensson, S. O., Hanfland, M., Fitch, A. N. & Hausermann, D. Two-dimensional detector software: from real detector to idealised image or two-theta scan. *High Press. Res.* **14,** 235–248 (1996).
51. Juhas, P., Davis, T., Farrow, C. L. & Billinge, S. J. L. PDFgetX3: a rapid and highly automatable program for processing powder diffraction data into total scattering pair distribution functions. *J. Appl. Crystallogr.* **46,** 560–566 (2013).
52. Farrow, C. L. *et al*. PDFfit2 and PDFgui: computer programs for studying nanostructure in crystals. *J. Phys.: Condens. Matter.* **19,** 335219 (2007).
53. Liu, Y., He, S., Uehara, M. & Maeda, H. Wet chemical preparation of well-dispersed colloidal cerium oxide nanocrystals. *Chem. Lett.* **36,** 764–765 (2007).